

# Spatially resolved observations of outflows in the radio loud AGN of UGC 8782

Rogemar A. Riffel <sup>1,★</sup>, Rogério Riffel <sup>2</sup>, Marina Bianchin <sup>1,3</sup>, Thaisa Storchi-Bergmann,<sup>2</sup> Gabriel Luan Souza-Oliveira<sup>1</sup> and Nadia L. Zakamska <sup>4</sup>

<sup>1</sup>*Departamento de Física, CCNE, Universidade Federal de Santa Maria, 97105-900 Santa Maria, RS, Brazil*

<sup>2</sup>*Departamento de Astronomia, IF, Universidade Federal do Rio Grande do Sul, CP 15051, 91501-970 Porto Alegre, RS, Brazil*

<sup>3</sup>*Department of Physics and Astronomy, University of California, 4129 Frederick Reines Hall, Irvine, CA 92697, USA*

<sup>4</sup>*Department of Physics & Astronomy, Bloomberg Center, Johns Hopkins University, 3400 N. Charles St, Baltimore, MD 21218, USA*

Accepted 2023 March 13. Received 2023 March 13; in original form 2022 November 3

## ABSTRACT

We use optical integral field spectroscopy (IFU) to study the gas emission structure and kinematics in the inner  $3.4 \times 4.9$  kpc<sup>2</sup> region of the galaxy UGC 8782 (3C 293), host of a radio loud active galactic nucleus (AGN). The observations were performed with the Gemini-North multi-object spectrograph (GMOS)-IFU on the Gemini North telescope, resulting in a spatial resolution of  $\sim 725$  pc at the distance of the galaxy. While the stars present ordered rotation following the orientation of the large-scale disc, the gas shows a disturbed kinematics. The emission-line profiles present two kinematic components: a narrow ( $\sigma \lesssim 200$  km s<sup>-1</sup>) component associated with the gas in the disc of the galaxy and a broad ( $\sigma \gtrsim 200$  km s<sup>-1</sup>) component produced by gas outflows. Emission-line ratio diagrams indicate that the gas in the disc is excited by the AGN radiation field, while the emission of the outflow includes additional contribution of shock excitation due to the interaction of the radio jet with the environment gas. Deviations from pure rotation, of up to 30 km s<sup>-1</sup>, are observed in the disc component and likely produced by a previous merger event. The broad component is blueshifted by  $\sim 150$ – $500$  km s<sup>-1</sup> relative to the systemic velocity of the galaxy in all locations. We construct radial profiles of the mass outflow rate and kinetic power of the ionized gas outflows, which have the maximum values at  $\sim 1$  kpc from the nucleus with peak values of  $\dot{M}_{\text{out},\Delta R} = 0.5 \pm 0.1 M_{\odot} \text{ yr}^{-1}$  and  $\dot{K}_{\text{out},\Delta R} = (6.8 \pm 1.1) \times 10^{41} \text{ erg s}^{-1}$ . The kinetic coupling efficiency of these outflows are in the range of 1–3 per cent, indicating that they could be powerful enough to affect the star formation in the host galaxy as predicted by theoretical simulations.

**Key words:** galaxies: active – galaxies: individual: UGC 8782 (3C 293) – galaxies: kinematics and dynamics.

## 1 INTRODUCTION

Feedback from active galactic nuclei (AGNs) is claimed to play a major role in shaping massive galaxies, by quenching star formation and transforming them from star-forming to quiescent galaxies (e.g. Di Matteo, Springel & Hernquist 2005; Fabian 2012; Kormendy & Ho 2013; Harrison et al. 2018). A critical ingredient in the rapid quenching of star formation in AGN hosts is multiphase gas outflows, which can push gas out of the galaxy or redistribute it, preventing it from collapsing to form stars. However, understanding the acceleration mechanisms of such outflows remains an important unknown piece of the galaxy evolution puzzle. This question can be addressed by spatially resolved observations of tracers of the multiple gas phases of AGN-driven winds (e.g. Riffel et al. 2006; Feruglio et al. 2010, 2015; Liu et al. 2013; May & Steiner 2017; Ramos Almeida et al. 2017; Rupke et al. 2019; Shimizu et al. 2019; Couto et al. 2020; Riffel et al. 2020b, 2023; Comerón et al. 2021; Dall’Agnol de Oliveira et al. 2021; Riffel 2021; Ruschel-Dutra et al. 2021; Speranza et al. 2022).

Using a sample composed of all galaxies in the entire spectroscopic data base of the *Spitzer Space Telescope*, Lambrides et al. (2019) found that AGN hosts show a significant excess of H<sub>2</sub> emission compared with the expected emission from star formation in normal photodissociation regions. In a following up work, Riffel, Zakamska & Riffel (2020a) cross-correlated the sample of Lambrides et al. (2019) with the SDSS-III data base. One important result of this work is that the excess of H<sub>2</sub> emission appears to be strongly related to both emission-line and kinematic shock diagnostics, such as [O I]  $\lambda 6300$  flux and velocity dispersion – as shown in Fig. 1. These results suggest that the H<sub>2</sub> emission excess originates from wind-driven shocks in neutral and molecular gas (Hill & Zakamska 2014). These conclusions were based on single aperture spectra. Spatially resolved observations of the neutral and ionized gas emission can provide indirect information about the role of AGN winds in the production of the H<sub>2</sub> emission excess in the mid-infrared.

It is very difficult to accelerate dense clouds of molecular gas up to velocities high enough to escape galaxies without them being fragmented and the molecules dissociated by the intense radiation field of the AGN. Recent theoretical models suggest that molecules may be formed inside the wind, and their emission may be produced by shock heating of the gas (Richings & Faucher-Giguère 2018a,b). The CO emission is commonly used as a tracer of cold molecular

\* E-mail: rogemar@ufsm.br

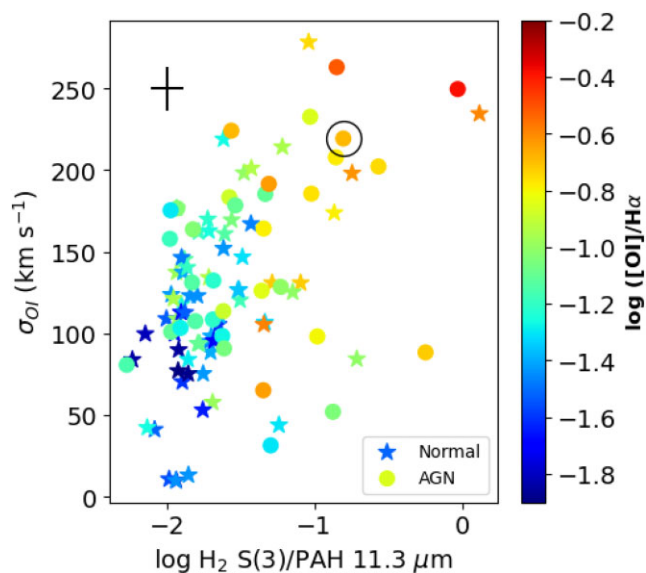


**Figure 1.** [O I] velocity dispersion versus the  $\text{H}_2\text{S}(3)/\text{PAH}\lambda 11.3\ \mu\text{m}$  intensity line ratio for the matched Spitzer-SDSS sample from Riffel et al. (2020a). The points are colour coded according to the [O I]  $\lambda 6300/\text{H}\alpha$  values as indicated by the colour bar. AGN hosts are shown as filled circles, while normal galaxies are represented by stars. Typical uncertainties are shown in the top-left corner and the open circle represents UGC 8782.

( $T \sim 100\ \text{K}$ ) outflows in AGN hosts (e.g. Alonso-Herrero et al. 2019), while the hot molecular phase ( $T > 1000\ \text{K}$ ) can be studied via the  $\text{H}_2$  near-infrared emission lines (e.g. Davies et al. 2014; Fischer et al. 2017; Riffel et al. 2021c; Bianchin et al. 2022). Not much is known about the warm molecular phase ( $T \sim 200\text{--}1000\ \text{K}$ ) traced by the  $\text{H}_2$  emission in the mid-infrared, which can be studied in a spatially resolved way only now with the JWST. As such observations are very time demanding, it is essential to choose carefully the objects to be studied.

Here, we present optical integral field unit (IFU) observations of the central region of the galaxy UGC 8782, which are used to map the neutral and ionized gas emission structure and kinematics. This object was selected as a likely host of strong molecular outflow, by being among the galaxies with the highest values of  $\text{H}_2\text{S}(3)/\text{PAH}\lambda 11.3\ \mu\text{m}$ , [O I]  $\lambda 6300/\text{H}\alpha$  intensity line ratios, and [O I]  $\lambda 6300$  velocity dispersion in the sample of Riffel et al. (2020a). It is identified by a circle in Fig. 1 and direct observations of the warm molecular hydrogen emission will be obtained as part of an approved cycle 1 JWST proposal (Proposal 1928, PI: Riffel, R. A.).

UGC 8782 (3C 293) at a redshift of  $z = 0.045$  (Sandage 1966) is a radio loud source (Liu & Zhang 2002) with nuclear activity classified as a low-ionization nuclear emission region (LINER; Véron-Cetty & Véron 2006). Optical images reveal complex morphology with filamentary dust lanes at hundreds of parsecs and kpc scales, likely as a result of a merger event (e.g. Martel et al. 1999). This galaxy presents a double-double radio source, with 200 kpc outer lobes oriented approximately along the north-west–south-east direction and  $\sim 4$  kpc scale inner lobes along the east–west direction (e.g. Machalski et al. 2016). Outflows from the nucleus of UGC 8782 were observed in neutral hydrogen, with velocities of up to  $1400\ \text{km s}^{-1}$ , coming from the western radio hotspot (Morganti et al. 2003; Mahony et al. 2013) and in ionized gas, but with the highest velocities, of up to  $1000\ \text{km s}^{-1}$ , co-spatial with the eastern radio knot, at the opposite side of the neutral gas outflows (Emonts et al. 2005; Mahony et al. 2016). These outflows have been interpreted by the

authors as being produced by the interaction of the radio jet with the interstellar medium. Kukreti et al. (2022) combined multifrequency radio data of 3C 293, obtained with the international low-frequency radio telescope, multi-element radio linked interferometer network (MERLIN) and very large array, to map the spectral index over a broad frequency range. They found that the inner radio lobes are part of a young jet-dominated radio source strongly interacting with the interstellar medium, likely driven by the ionized outflows mentioned above. By comparing the spectral indices of the inner radio structure to that from the structures at larger scales, the authors conclude that 3C 293 underwent at least two episodes of nuclear activity.

This paper is organized as follows: Section 2 presents the observations and data reduction procedure, while Section 3 describes the emission line fitting and stellar kinematics measurements. The results are presented in Section 4 and discussed in Section 5, and Section 6 summarizes our conclusions. We adopt a redshift-based distance to UGC 8782 of 200 Mpc, for which 1 arcsec corresponds to  $\sim 970$  pc at the galaxy.

## 2 OBSERVATIONS AND DATA REDUCTION

UGC 8782 was observed on 2022 February 23 with the Gemini-North Multi-Object Spectrograph (GMOS; Hook et al. 2004) operating in the IFU (Allington-Smith et al. 2002) mode, under the program code GN-2022A-Q-310 (PI: Riffel, R. A.). We used B600-G5323 grating and the one-slit mode of the GMOS-IFU, which provides a field of view of  $3.5\ \text{arcsec} \times 5.0\ \text{arcsec}$ . The observations of UGC 8782 were split into six exposures of 1200 s, half centred at  $6250\ \text{\AA}$  and half at  $5950\ \text{\AA}$ , in order to account for the detector gaps.

The data reduction was performed with the GEMINI.GMOS package with the IRAF software following the standard procedures for spectroscopic data, which includes the subtraction of the bias level, trimming and flat-field correction, background subtraction for each science data, quantum efficiency correction, sky subtraction and wavelength calibration. The LACOS algorithm (van Dokkum 2001) was used for cosmic rays removal and finally we performed the flux calibration, using observations of the standard star Feige 66 to construct the sensitivity function. The final data cubes for each individual exposure have an angular sampling of  $0.1\ \text{arcsec} \times 0.1\ \text{arcsec}$ .

The final data cube for UGC 8782 was obtained by median combining the individual exposure data cubes using the peak of the continuum as reference for astrometry corrections among individual cubes. The final data cube covers the spectral region from 4650 to  $7500\ \text{\AA}$ , which includes the most prominent optical emission lines seen in AGN spectra, from  $\text{H}\beta$  to [S II]  $\lambda 6731\ \text{\AA}$ . The velocity resolution is  $\approx 80\ \text{km s}^{-1}$  as estimated from the full width at half-maximum (FWHM) of typical emission lines in the CuAr spectra used in the wavelength calibration and the angular resolution is  $\sim 0.75$  arcsec as estimated from the FWHM field stars in the UGC 8782 acquisition image, corresponding to the  $\sim 725$  pc at the distance of the galaxy.

## 3 MEASUREMENTS

### 3.1 Stellar kinematics

We use the Penalized Pixel-Fitting (PPXF) method (Cappellari & Emsellem 2004; Cappellari 2017, 2022) to fit and subtract the stellar component from the observed spectra. The code finds the best fit of the observed spectra by convolving template spectra with the line-of-sight velocity distribution assumed to be reproduced by Gauss–Hermite series. We fit the whole spectral region, masking out regions

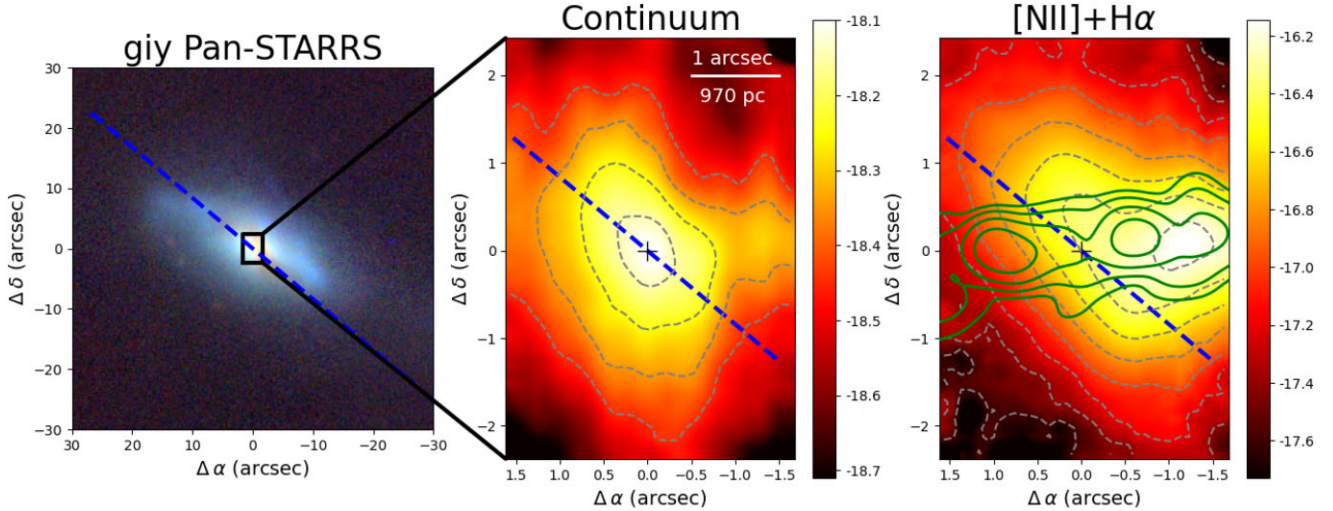


**Figure 2.** Left: composite image of the 1 arcmin  $\times$  1 arcmin *g* (4866 Å), *i* (4866 Å), and *y* (9633 Å) bands of UGC 8782 from Pan-STARRS data archive (Chambers et al. 2016; Flewelling et al. 2016). Middle: GMOS 6100 Å continuum image. The colour bar shows the continuum flux values in logarithmic units of  $\text{erg s}^{-1} \text{cm}^{-2} \text{Å}^{-1}$ . Right: [NII] + H $\alpha$  narrow-band image obtained from the GMOS data cube. The colour bar shows the flux values in logarithmic units of  $\text{erg s}^{-1} \text{cm}^{-2}$ . The blue dashed lines show the orientation of the galaxy major axis as obtained from the 2MASS *K*-band image (Skrutskie et al. 2006) and the central crosses mark the position of the nucleus, defined as the location of the peak of the continuum emission. The green contours overlaid to the [NII] + H $\alpha$  image show the inner radio structure of UGC 8782 at 1360 MHz presented by Kukreti et al. (2022). In all images, North is up and East is to the left.

of strong emission lines and use as spectral templates those from the MILES-HC library (Westfall et al. 2019), which has a similar spectral resolution of our GMOS data. We allow PPXF to include multiplicative fifth-order polynomials to further adjust the continuum shape of the template to the observed spectra. In addition, we use the *clean* parameter of PPXF to use the iterative sigma clipping method described in Cappellari et al. (2002) to reject spectral pixels that deviate more than  $3\sigma$  from the best fit, in order to exclude from the fit unmasked bad pixels, due to remaining sky lines and spurious features.

The output from the PPXF code includes measurements of the radial velocity ( $V_*$ ) and stellar velocity dispersion ( $\sigma_*$ ) at each spaxel, which are used to construct two-dimensional maps presented in Fig. 3. In addition, we subtract the best-fitting model at each spaxel from the observed spectra in order to produce a data cube free of the stellar population component, which is used to measure the emission-line properties.

### 3.2 Emission-line fitting

We use the IFSCUBE package (Ruschel-Dutra & de Oliveira 2020; Ruschel-Dutra et al. 2021) to fit the observed emission-line profiles by Gaussian curves. The fit is performed after the subtraction of the stellar component contribution from the observed spectra, and we allow the code to include two Gaussian curves (*a narrow* and *a broad* component) per emission line, as indicated by visual inspection of the spectra. We use the CUBEFIT routine from the IFSCUBE package and fit the following emission lines simultaneously: H $\beta$ , [O III]  $\lambda\lambda 4959, 5007$ , [O I]  $\lambda 6300$ , [N II]  $\lambda\lambda 6548, 6583$ , H $\alpha$  and [S II]  $\lambda\lambda 6717, 6731$ . Initial guesses of the Gaussian amplitude, centroid velocity, and velocity dispersion are provided to the code based on measurements of the nuclear spectrum using the *splot* IRAF task, which are used to fit the nuclear spectrum. After a successful fit of the nuclear emission line profiles, the routine fits the surrounding spaxels following a radial spiral loop, using as initial guesses the best-fitting parameters obtained from successful fits of spaxels at distances smaller than 0.3 arcsec from the fitted spaxel, as defined

by using the *refit* parameter. If the amplitude of one of the fitted Gaussians is smaller than three times the standard deviation of the nearby continuum, only one component is used. To account for possible remaining continuum emission, we also include fourth-order polynomial, which is used to fit the continuum before the fitting of the emission lines.

During the fit, we tied the velocity and velocity dispersion ( $\sigma$ ) of emission lines produced from the same species (H $\beta$  and H $\alpha$ ; [O III]  $\lambda 5007$  and [O III]  $\lambda 4959$ ; [N II]  $\lambda 6548$  and [N II]  $\lambda 6583$ ; [S II]  $\lambda 6717$  and [S II]  $\lambda 6731$ ) for each kinematic component. We also fixed the [O III]  $\lambda 5007$ /[O III]  $\lambda 4959$  and [N II]  $\lambda 6583$ /[N II]  $\lambda 6548$  intensity line ratios of each component to their theoretical values of 2.98 and 3.06 (Osterbrock & Ferland 2006), respectively.

## 4 RESULTS

### 4.1 Spatially resolved observations

In Fig. 2, we present a large-scale *giy* image of UGC 8782 (left panel) from Pan-STARRS data archive (Chambers et al. 2016; Flewelling et al. 2016), along with a continuum (middle panel) and a [N II] + H $\alpha$  narrow band (right panel) image obtained from the GMOS data cube. The GMOS continuum image is obtained by computing the mean flux in a 100 Å window centred at 6100 Å. The blue dashed line shows the orientation of the galaxy's major axis (PA = 50°; Skrutskie et al. 2006). The continuum distribution is elongated along the north-east–south-west direction and has a smaller PA ( $\sim 35^\circ$  East of North) than for the large-scale disc, with a secondary extended structure observed to the west of the nucleus at  $\sim 1.3$  arcsec. The [N II] + H $\alpha$  narrow band image is obtained by integrating the fluxes within a spectral window from 6500 to 6640 Å – including these lines – using the cube with the contribution of the stellar population component subtracted. Extended gas emission is observed along the major axis of the galaxy, with a similar distribution as observed in the continuum. However, the strongest emission is observed at a structure located at 1.3 arcsec west from the nucleus.

Fig. 3 presents results for the stellar and gas kinematics and emission distributions. The stellar velocity field presents a velocity gradient consistent with the orientation of the major axis of the large-scale disc of PA = 50° (Skrutskie et al. 2006) with blueshifts seen to the south-west and redshifts to the north-east of the nucleus. The stellar velocity dispersion map presents values in the range from 100 to 270 km s<sup>-1</sup> with a mean value of 205 km s<sup>-1</sup> and standard deviation of 65 km s<sup>-1</sup>. Thus, the observed stellar kinematics in UGC 8782 is consistent with the behaviour expected for a rotation disc with similar orientation of the large-scale disc of the galaxy.

The emission-line flux distributions for the narrow component are elongated along the local stellar disc, following a similar orientation of that of the major axis of the continuum image, for all emission lines, as can be seen in the first column of Fig. 3. The corresponding velocity fields also present a similar velocity behaviour of that in the stellar velocity field, with blueshifts to the south-west and redshifts to the north-east. The gas velocity dispersion maps for the narrow component for all emission lines present values smaller than those observed for the stars, with values lower than 150 km s<sup>-1</sup> at most locations. The kinematics and emission structure of the narrow component are consistent with emission of gas in a rotating disc, similarly to that observed for the stars. The slightly larger velocity amplitude and smaller velocity dispersion values observed for the gas as compared with those of the stars can be explained by projection effects if the gas is located in a thin disc and the stars in a thicker distribution.

The broad component emission is extended mostly to the west of the nucleus for all emission lines. The emission peaks at ~1 arcsec west of the nucleus are close to the border of a radio knot observed at 0.7 arcsec west. The centroid velocity of the broad component is blueshifted by about 200 km s<sup>-1</sup> and the  $\sigma$  maps present values of up to 400 km s<sup>-1</sup>. The green contours overlaid to the H $\alpha$  flux distribution and  $\sigma$  map for the broad component are from the 1360 MHz radio image obtained with the MERLIN array and presented by Kukreti et al. (2022). The highest fluxes for the broad components are observed co-spatially with the radio structure to the west and the highest velocity dispersion values are seen surrounding the western radio lobe, suggesting that the emission of the broad component is associated with the interaction of the radio jet with the ambient gas.

Following Riffel et al. (2021b), we estimate the visual extinction ( $A_V$ ) using the H $\alpha$ /H $\beta$  intensity line ratio, by

$$A_V = 7.22 \log \left[ \frac{(F_{H\alpha}/F_{H\beta})_{\text{obs}}}{2.86} \right], \quad (1)$$

where  $(F_{H\alpha}/F_{H\beta})_{\text{obs}}$  is the observed H $\alpha$ /H $\beta$  flux ratio, adopting the Cardelli, Clayton & Mathis (1989) extinction law and an intrinsic flux ratio of  $F_{H\alpha}/F_{H\beta} = 2.86$  for H I case B recombination for an electron temperature of  $T_e = 10\,000$  K and electron density of  $N_e = 100$  cm<sup>-3</sup> (Osterbrock & Ferland 2006). The resulting maps for the narrow and broad-line components are shown, respectively, in the top and bottom panels of Fig. 4. The  $A_V$  map for the narrow component shows values in the range from 0 to 3.5 mag, with the highest ones seen at the north-west side of the galaxy, co-spatial with the dust structure seen in the large-scale image of Fig. 2. The mean value is  $\langle A_V \rangle = 2.7 \pm 0.1$  mag. The broad component in the H $\beta$  emission line is detected only in a few spaxels and thus its resulting  $A_V$  map shows a limited spatial coverage. The mean value for the broad component is  $\langle A_V \rangle = 1.7 \pm 0.4$  mag.

The central panels of Fig. 4 show the [S II]  $\lambda 6717$ /[S II]  $\lambda 6731$  flux ratio maps for UGC 8782 for the narrow (top) and broad (bottom) components. For the narrow component, the lowest values of ~0.9

are seen to the south-west of the nucleus, while the highest values of up to 1.6 are observed mostly to the north-west and north of the nucleus. For the broad component, the lowest values of ~0.9 are seen to the west of the nucleus, close to the tip of the radio jet, while higher values of up to 2.6 are seen to the south. The [S II]  $\lambda 6717$ /[S II]  $\lambda 6731$  ratio can be used to estimate the electron density ( $N_e$ ) for intensity line ratios in the range of ~0.5–1.4 (Osterbrock & Ferland 2006). Higher values of [S II]  $\lambda 6717$ /[S II]  $\lambda 6731$  are produced in lower density gas, while lower ratios are associated with higher density clouds.

To estimate the electron density of the emitting gas for both kinematic components, we used the PYNEB python package (Luridiana, Morisset & Shaw 2015) and assume an electron temperature of  $1.5 \times 10^4$  K, a typical value observed in Seyfert nuclei (Revalski et al. 2018a,b, 2021; Dors et al. 2020; Riffel et al. 2021a,d). The resulting  $N_e$  maps are shown in the right panels of Fig. 4. The map for the narrow component presents the highest values ( $> 1700$  cm<sup>-3</sup>) to the south-west of the nucleus and the lowest values ( $< 200$  cm<sup>-3</sup>) to the north-east, and a mean value of  $\langle N_e \rangle = 607 \pm 27$  cm<sup>-3</sup>. Most locations with detection of the broad component in the [S II] doublet present ratios larger than 1.4, where the relation between the line ratio and  $N_e$  becomes flat (Osterbrock & Ferland 2006). These regions correspond to very low densities ( $\lesssim 50$  cm<sup>-3</sup>). The highest densities ( $\sim 1600$  cm<sup>-3</sup>) are found close to the edge of the radio jet to the west of the nucleus and the mean value is  $\langle N_e \rangle = 740 \pm 72$  cm<sup>-3</sup>.

Emission-line ratio diagrams can be used to identify the dominant gas ionization source in a galaxy. In the optical, the BPT (Baldwin, Phillips & Terlevich 1981) and WHAN (Cid Fernandes et al. 2010, 2011) diagrams are commonly used for this purpose. In the top panels of Fig. 5, we present the spatially resolved [O III]  $\lambda 5007$ /H $\beta$  versus [N II]  $\lambda 6583$ /H $\alpha$  BPT diagram using the fluxes of the narrow-line component, as well as a colour-coded excitation map (right). The grey regions in the excitation map correspond to locations where at least one line is not detected above the  $3\sigma$  threshold. Most spaxels with detected emission in all four lines show ratios in the regions occupied by LINERs and transition objects (TOs). The blue triangle shown in the BPT diagram corresponds to the nucleus, as obtained using the line fluxes computed within a circular aperture of 0.5 arcsec radius. The broad component of [O III]  $\lambda 5007$  and H $\beta$  is detected only in a few spaxels around the position of its emission peak (1.0 arcsec west of the nucleus) and thus we do not present its BPT diagram, but we compute the integrated fluxes within a 0.5 arcsec radius aperture centred at 1.0 arcsec west of the nucleus. The ratios for the narrow and broad components integrated within this aperture are shown as a black square and a black star, respectively.

The WHAN diagrams for the narrow and broad components are shown in the middle and bottom panels of Fig. 5, along with their corresponding excitation maps. The WHAN diagram is particularly useful to separate emission of gas ionized by an AGN – which results in H $\alpha$  equivalent widths,  $EW_{H\alpha} > 3 \text{ \AA}$  – from those that can be attributed to hot low-mass evolved stars (HOLMES) with  $EW_{H\alpha} < 3 \text{ \AA}$  (Cid Fernandes et al. 2010, 2011; Agostino et al. 2021). The WHAN diagrams for UGC 8782 show that most points are located in the regions occupied by AGNs, and emission of gas excited by HOLMES can be neglected.

UGC 8782 presents [O I]  $\lambda 6300$  extended emission over most of the GMOS field of view. This emission line can be used as a tracer of shocks in neutral gas (e.g. Allen et al. 2008; Ho et al. 2014; Riffel et al. 2020a). In Fig. 6, we present plots of the [O I] velocity dispersion ( $\sigma_{O I}$ ) versus the [O I]  $\lambda 6300$ /H $\alpha$  flux line ratio using measurements

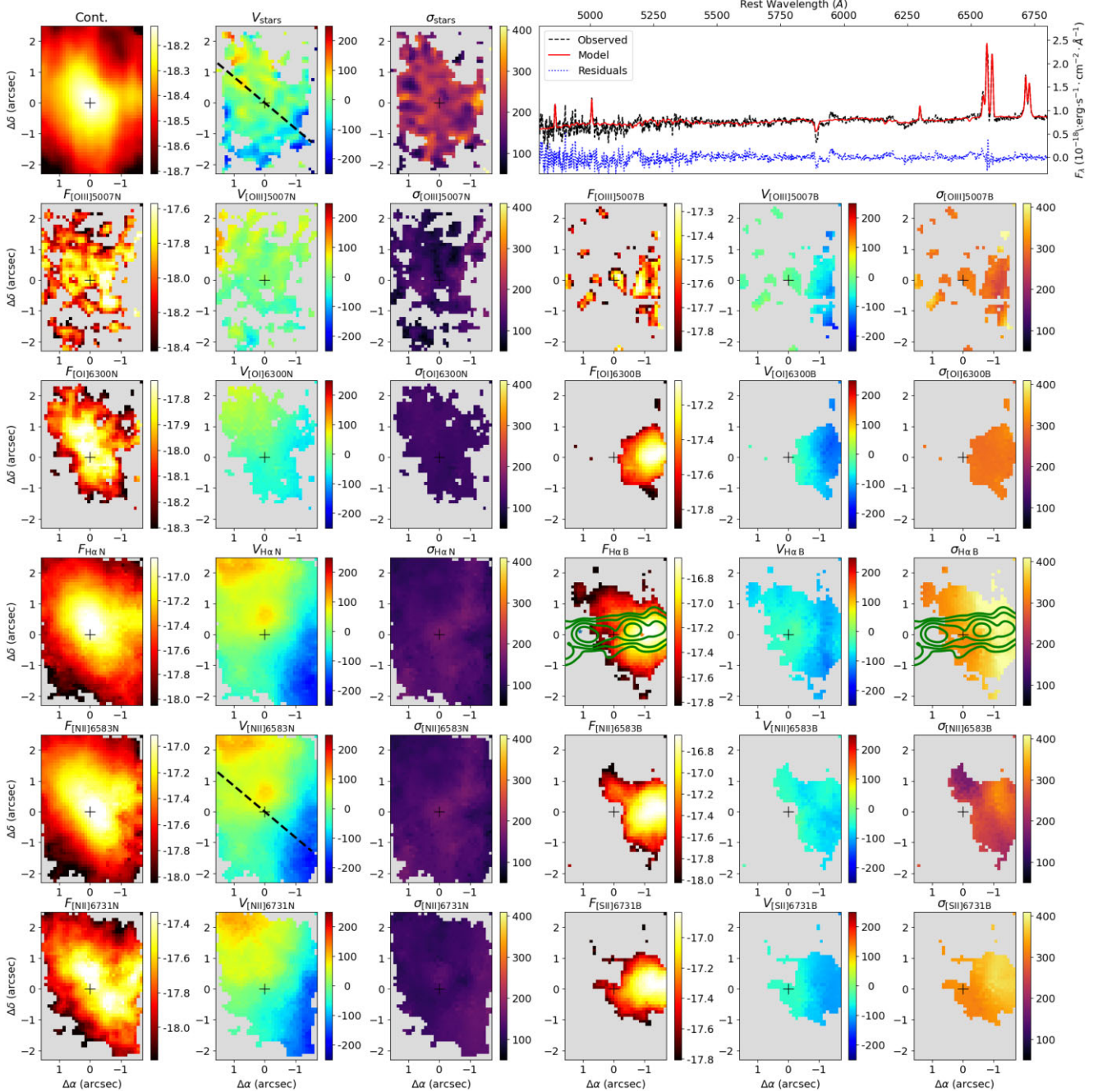


**Figure 3.** Stellar and gas kinematics and distribution in UGC 8782. The first row shows, from left to right, a continuum image obtained by computing the mean fluxes from the GMOS cube within a  $100 \text{ \AA}$  window centred at  $6000 \text{ \AA}$ , the stellar velocity field, stellar velocity dispersion map, and an example of fitting procedure for the nuclear spaxel. The observed nuclear spectrum is shown as a black dashed line, the best-fitting model is represented in red, and the residual (plus an arbitrary constant) is shown as a dotted line. The remaining rows show the results for the  $[\text{O III}] \lambda 5007$ ,  $[\text{O I}] \lambda 6300$ ,  $\text{H}\alpha$ ,  $[\text{N II}] \lambda 6583$ , and  $[\text{S II}] \lambda 6731$  emission lines, from top to bottom. For each emission line, we show, from left to right, the flux distribution, centroid velocity, and velocity dispersion maps for the narrow (first three panels) and broad (last three panels) components. The colour bars show the line fluxes in logarithmic units of  $\text{erg s}^{-1} \text{ cm}^{-2} \text{ spaxel}^{-1}$ , the velocity and velocity dispersion maps in  $\text{km s}^{-1}$ , and the continuum image in logarithmic units of  $\text{erg s}^{-1} \text{ cm}^{-2} \text{ \AA}^{-1} \text{ spaxel}^{-1}$ . The central crosses mark the position of the nucleus, defined as the location of the continuum peak and in all panels the North is up and East to the left. The green contours overlaid in some panels are from the 1360 MHz radio image of UGC 8782 presented by Kukreti et al. (2022). The black dashed lines show the orientation of the galaxy’s major axis (position angle (PA) =  $50^\circ$ ; Skrutskie et al. 2006). Grey regions in the stellar kinematic maps correspond to locations with velocity or  $\sigma$  uncertainties larger than  $50 \text{ km s}^{-1}$ , while in the emission-line maps these regions correspond to locations where the corresponding emission-line density flux is not detected above three times the standard deviation of the spectra noise, computed in neighbouring spectral regions of each emission line.

for the narrow (left panel) and broad (right panel) components. The narrow component presents  $100 \text{ km s}^{-1} \lesssim \sigma_{01} \lesssim 130 \text{ km s}^{-1}$  and  $-1.0 \lesssim \log([\text{O I}]/\text{H}\alpha) \lesssim -0.3$ , while for the broad component the ranges of values are  $290 \text{ km s}^{-1} \lesssim \sigma_{01} \lesssim 330 \text{ km s}^{-1}$  and  $-0.7$

$\lesssim \log([\text{O I}]/\text{H}\alpha) \lesssim 0.0$ . The black points correspond to mean values computed within bins of  $0.05 \text{ dex}$  in  $\log [\text{O I}] \lambda 6300/\text{H}\alpha$ , and the error bars represent the standard deviation of the velocity dispersion within each bin.

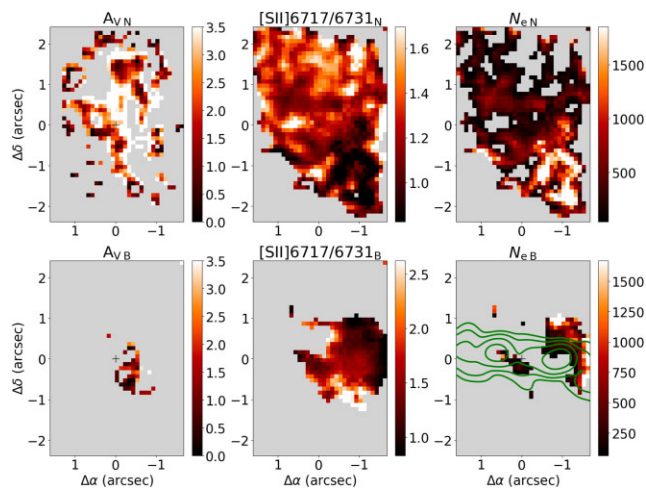


**Figure 4.** Visual extinction (left) in magnitudes, [S II]  $\lambda 6717$ /[S II]  $\lambda 6731$  intensity line ratio (middle), and electron density (right) maps for the narrow (top) and broad (bottom) components, in units of  $\text{cm}^{-3}$ . The grey regions correspond to locations where one of both emission lines used in the ratio is not detected above  $3\sigma$  continuum noise. The green contours overlaid in some panels are from the 1360 MHz radio image of UGC 8782 presented by Kukreti et al. (2022).

#### 4.2 Integrated spectra at selected positions

Previous observations of UGC 8782 revealed broad emission line components associated with the eastern radio jet, with higher velocities and much fainter emission, as compared with the broad components seen to the west of the nucleus (Mahony et al. 2016). These authors interpreted this result as the broad components originating from a bipolar outflow, driven by the radio jet. As shown in the previous section, we do not detect this eastern broad component above  $3\sigma$  noise level in individual spaxels, but there is some extended emission to the north of the nucleus as observed for  $H\alpha$  and [N II]  $\lambda 6583$  emission lines (Fig. 3). In order to investigate the origin of the broad component, we have extracted individual spectra within circular apertures of 0.4 arcsec radius (comparable to the seeing of the observations) centred at five positions: (i) the nucleus; (ii) the location of the western radio hotspot ( $\Delta\alpha = -1.1$  arcsec;  $\Delta\delta = 0.1$  arcsec); (iii) the location of the eastern radio hotspot ( $\Delta\alpha = 0.9$  arcsec;  $\Delta\delta = 0.0$  arcsec); (iv) 1.0 arcsec north of the nucleus; (v) and 1.0 arcsec south of the nucleus. The resulting spectra are shown as black dashed lines in Fig. 7 and reveal the presence of broad-line components in all locations, not only along the radio jet. We followed the same procedure described above and fitted each emission line by two Gaussian curves using the IFSCUBE package, keeping the kinematics (velocity and  $\sigma$ ) of the narrow and broad components tied, separately. The resulting models are shown in red in Fig. 7 and the individual components are shown as green dotted and blue dashed-dotted lines, respectively.

As in Mahony et al. (2016) – who used optical integral field spectrograph (OASIS) observations of UGC 8782 with the William Herschel Telescope (WHT) – we also find that the broad component emission in the western radio hotspot position is about one order of magnitude brighter than that in the eastern hotspot region. In addition, our GMOS data reveal broad component emission in regions perpendicular to the radio jet, as seen in the spectra extracted in regions to the north and to the south of the nucleus in Fig. 7. The broad component emission in these regions is stronger than those in the eastern radio hotspot location by a factor of 2, for example,

when  $H\alpha$  line is considered. The broad component is blueshifted in all locations with velocities of  $-450 \pm 48 \text{ km s}^{-1}$  for the nucleus,  $-200 \pm 57 \text{ km s}^{-1}$  (for the eastern hotspot),  $-175 \pm 30 \text{ km s}^{-1}$  (western hotspot),  $-140 \pm 38 \text{ km s}^{-1}$  (1.0 arcsec south), and  $-365 \pm 40 \text{ km s}^{-1}$  (1.0 arcsec north). The widths of the broad component are in the range of  $380\text{--}560 \text{ km s}^{-1}$ , with the lowest value observed at the south of the nucleus and the highest at the eastern radio hotspot.

In addition, in Fig. 7 we present the  $W_{80}$  map for the  $H\alpha$  emission line. This parameter corresponds to the width of the line profile containing 80 percent of its total flux and can be used to identify gas outflows that typically present  $W_{80} > 500 \text{ km s}^{-1}$  observed in the [O III]  $\lambda 5007$  emission line (e.g. Zakamska & Greene 2014; Wylezalek et al. 2020; Ruschel-Dutra et al. 2021). The  $W_{80}$  map for UGC 8782 presents values larger than this threshold at several locations surrounding the nucleus, with the highest values of up to  $900 \text{ km s}^{-1}$  seen to the west of the nucleus along the radio jet.

## 5 DISCUSSION

Mahony et al. (2016) used optical integral field spectroscopy, obtained with the OASIS-IFU on the 4.2 m WHT, to study the gas kinematics in the inner  $12 \times 9 \text{ arcsec}^2$  of UGC 8782. Their observations covered the [N II] +  $H\alpha$  and the [S II] doublet emission lines with angular sampling ranging from  $0.3 \text{ arcsec} \times 0.3 \text{ arcsec}$  in the central regions to  $3.6 \text{ arcsec} \times 2.7 \text{ arcsec}$  in the outer regions. They detected a blueshifted broad component within the inner  $\approx 2 \text{ arcsec}$  along the east–west direction spanning the region between the inner radio lobes, slightly extended to the north of the nucleus. In addition, these authors analyse long-slit spectra along the positions angles  $225^\circ$  and  $93^\circ$ , previously published by Emonts et al. (2005), which show that the broad component is detected to distances of up to 5 kpc from the nucleus to both sides, along the radio jet. Although Mahony et al. (2016) do not present emission-line flux maps, they mention in their work that the broad component presents much higher peak fluxes in regions to the west of the nucleus, as compared with regions to the east of it. These authors interpret the broad component as being due to fast outflows driven by the radio jet, in an orientation such that the eastern side is approaching and the western side is receding. The eastern radio jet intercepts the disc, pushing the gas out and the radio jet creates a cocoon that disturbs the gas in all directions (Mahony et al. 2016).

Here, we use higher quality IFU data to further investigate the gas emission structure and kinematics. As in previous works, our GMOS data clearly reveal the presence of a narrow and a broad component, associated with gas emission from the disc and from the outflow. In the following, we will characterize both emission structures.

### 5.1 Origin of the gas emission

The nuclear emission of UGC 8782 was previously classified as a LINER based on optical line ratios, and interpreted as being produced by shock excitation (Emonts et al. 2005; Mahony et al. 2016). Our IFU data allow us to further investigate the origin of the gas emission, in a spatially resolved manner. The BPT diagram (Fig. 5) shows line ratios mostly in the region occupied by LINERs and TOs, with the nuclear emission being consistent with a LINER-type ionization. At the location of the western radio hotspot, the line ratios for the narrow component are also consistent with a LINER-type ionization and for the broad component, the observed line ratios are close

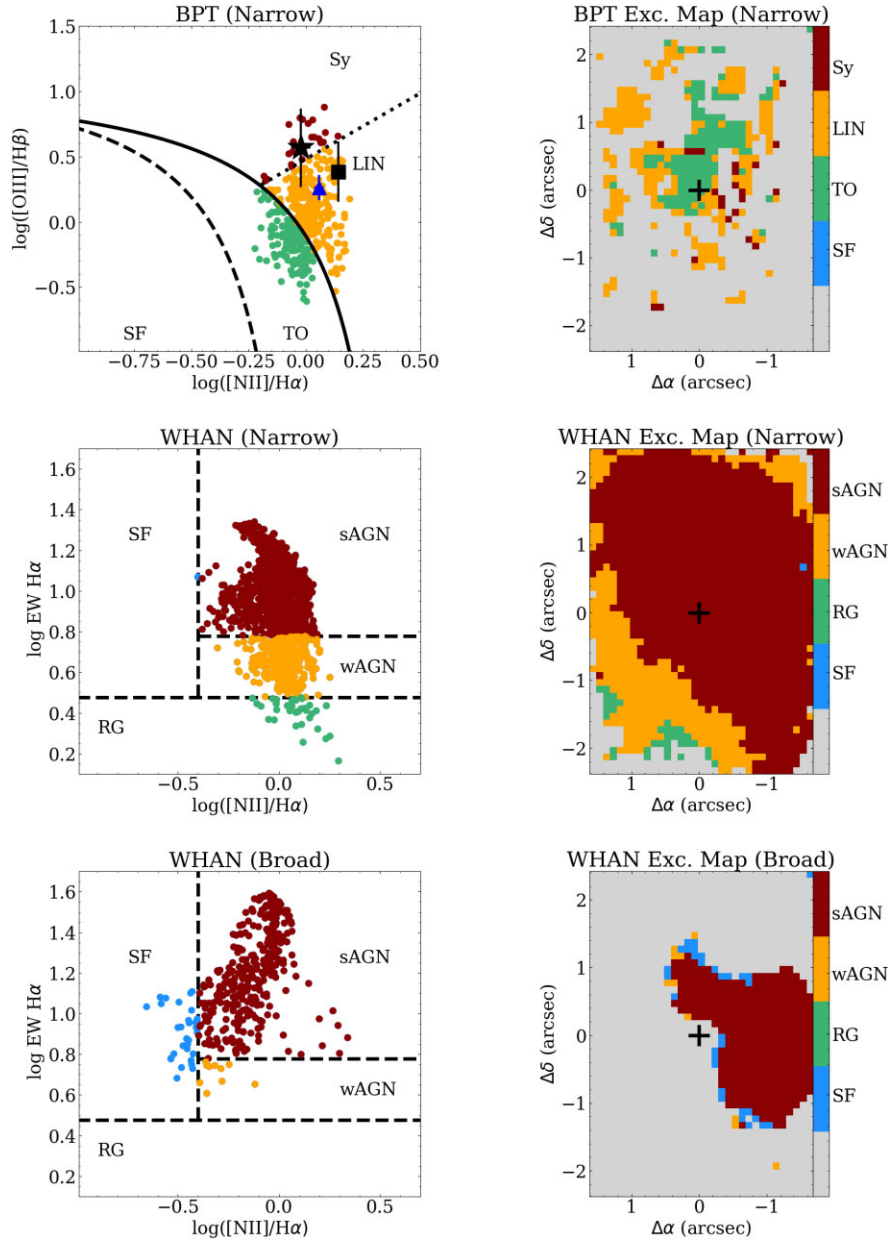


**Figure 5.** Spatially resolved BPT (Baldwin et al. 1981) and WHAN (Cid Fernandes et al. 2010, 2011) diagrams for UGC 8782. The top panels show the BPT diagram (left) and the colour-coded excitation map (right) for the narrow component. The continuous, dashed, and dotted lines are the borderlines from Kewley et al. (2001), Kauffmann et al. (2003), and Cid Fernandes et al. (2010), respectively. The blue triangle shows the values of the narrow component for a nuclear aperture of 0.5 arcsec radius. The black star and square represent the ratios measured within an aperture of 0.5 arcsec centred at 1.0 arcsec west of the nucleus (position of the emission peak of the broad component), for the broad and narrow components, respectively. We do not show the BPT diagram for the broad component because the [O III] and H  $\beta$  lines are detected only in a few spaxels. The middle and bottom panels show the WHAN diagrams and the corresponding excitation maps for the narrow and broad components, respectively. The lines in the WHAN diagram are those defined in Cid Fernandes et al. (2011) and the following nomenclature is used: star-forming galaxies (SF), transition objects (TO), weak AGN (wAGN; i.e. LINERs), strong AGN (sAGN; i.e. Seyferts), and retired galaxies (RG).

to the borderline separating Seyferts and LINERs in the WHAN diagram, as defined in Cid Fernandes et al. (2010). These results are consistent with the classification of UGC 8782 as a host of an AGN, based on the plot of the PAH<sub>6.2</sub>  $\mu\text{m}$  equivalent width ( $\text{EW}_{\text{PAH}6.2 \mu\text{m}}$ ) versus the H<sub>2</sub>S(3)/PAH11.3  $\mu\text{m}$  intensity line ratio using Spitzer data ( $\text{EW}_{\text{PAH}6.2 \mu\text{m}} \approx 0.09 \mu\text{m}$  and H<sub>2</sub>S(3)/PAH11.3  $\mu\text{m} \approx 0.15$  for UGC 8782; Lambrides et al. 2019).

Although the BPT and WHAN diagnostic diagrams are useful to separate photoionized gas by star-forming regions, AGN and

HOLMES, they are not sensitive to possible contributions from shocks (Agostino et al. 2021; Dors et al. 2021). The [O I]  $\lambda 6300/\text{H}\alpha$  intensity line ratio is a well-known tracer of shocks (Monreal-Ibero, Arribas & Colina 2006; Monreal-Ibero et al. 2010; Rich, Kewley & Dopita 2011, 2015). Shocks may be the dominant excitation mechanism of the [O I] emission if its velocity dispersion is larger than  $\sim 150 \text{ km s}^{-1}$  and  $\log [\text{O I}] \lambda 6300/\text{H}\alpha \gtrsim -1.0$  (e.g. Ho et al. 2014). The plots of  $\sigma_{\text{O I}}$  versus  $\log [\text{O I}] \lambda 6300/\text{H}\alpha$  shown in Fig. 6 reveal that, although  $\log [\text{O I}] \lambda 6300/\text{H}\alpha > -1.0$  for the disc component,

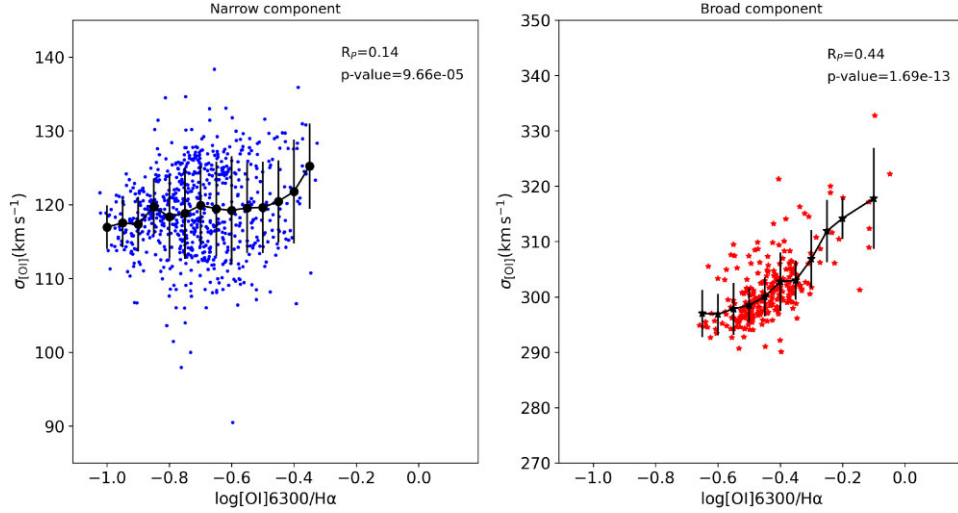


**Figure 6.** Plot of  $\sigma_{\text{OI}}$  versus  $\log [\text{O I}] \lambda 6300/\text{H}\alpha$  for the narrow (left) and broad (right) components. The black dots correspond to mean values computed within bins of 0.05 dex in  $\log [\text{O I}] \lambda 6300/\text{H}\alpha$ . The Pearson correlation coefficient ( $R_p$ ) and  $p$ -value are shown in the top-right corner of each panel.

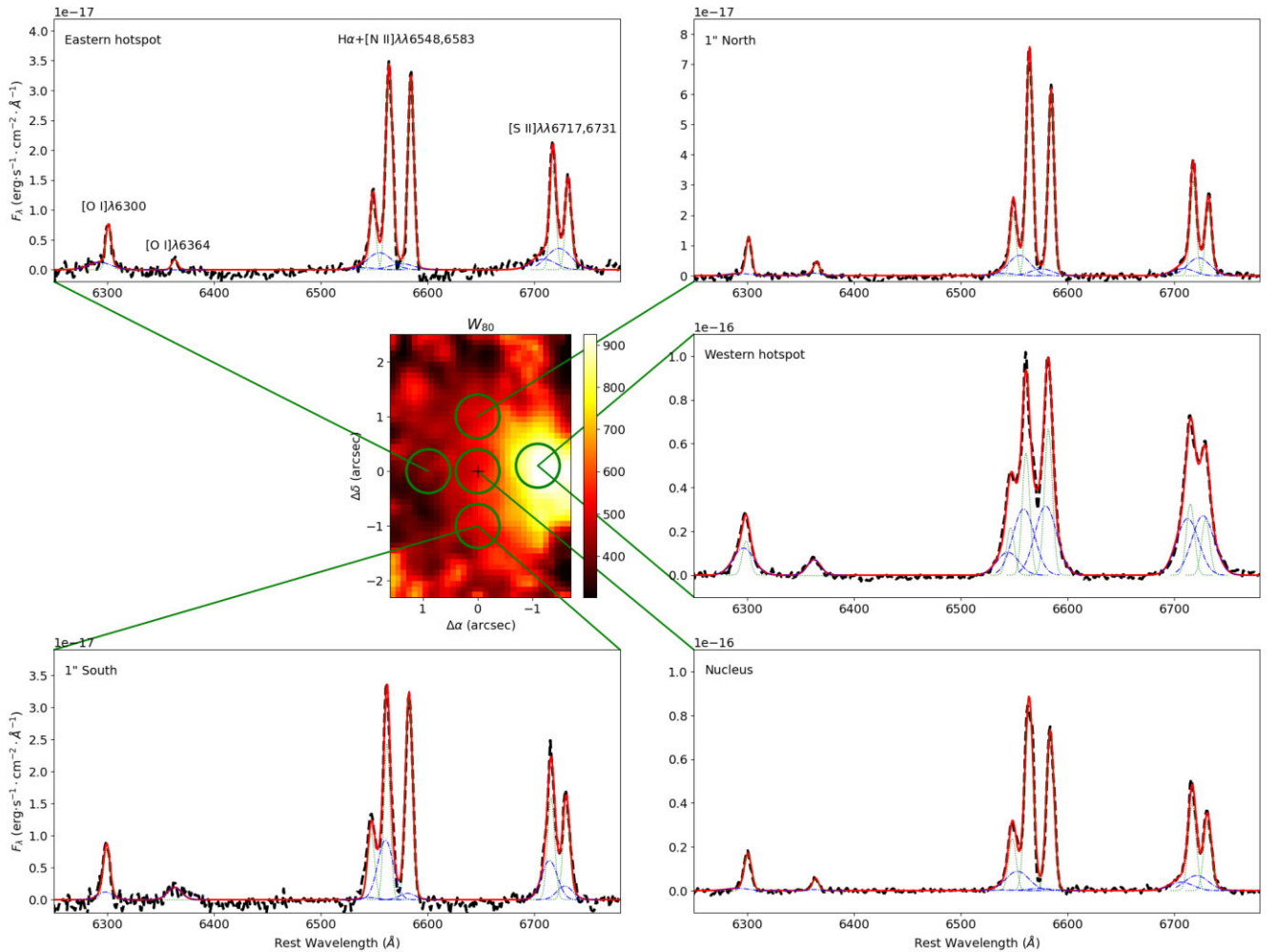


**Figure 7.** Fits of the emission lines in the red part of the spectra at five positions using integrated spectra extracted within 0.4 arcsec radii apertures, as represented by the green circles. The observed spectra with the stellar population contribution subtracted are shown in black and the best-fitting models in red. The individual components are shown as green dotted and blue dashed-dotted lines for the narrow and broad components, respectively. The central panel shows the  $W_{80}$  map for the  $\text{H}\alpha$  emission line, with the colour bar representing the values in  $\text{km s}^{-1}$ .



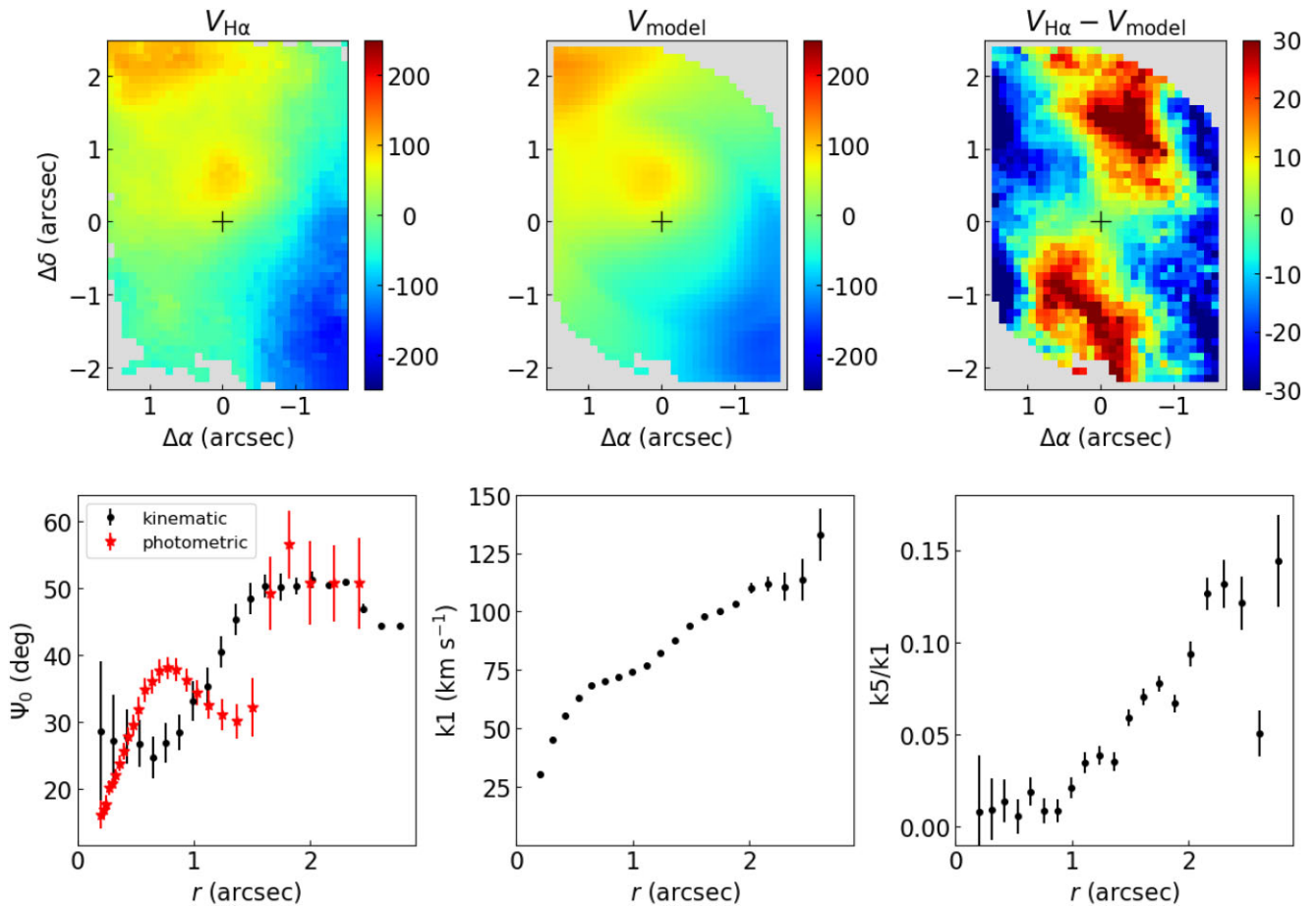


**Figure 8.** Top panels, from left to right: observed  $H\alpha$  velocity field for the narrow component, best-fitting model obtained with the KINEMETRY code, and residual velocity map, obtained by subtracting the model from the observed velocities. Bottom panels: the left panel shows plot of the PA of the major axis of the modelled ellipses along the radius. The black circles represent the kinematic PAs, and the red stars show the photometric PAs obtained by fitting the continuum image using the PHOTUTILS package. The central and right panels show the harmonic expansion coefficients  $k_1$  and  $k_5/k_1$  from the KINEMETRY model.

the velocity dispersion is low ( $100\text{--}130\text{ km s}^{-1}$ ), suggesting that photoionization may be the main mechanism in action. However, shocks with these velocities may also be able to excite the gas (Ho et al. 2014). Indeed, an additional contribution of shocks cannot be discarded as a weak correlation (Pearson correlation coefficient  $R_p = 0.14$ ) is observed between  $[\text{O I}]\lambda 6300/H\alpha$  and  $\sigma_{\text{O I}}$  for the narrow component. The highest values of both parameters are observed in regions along the disc, outside the AGN ionization cone. This result is consistent with the detection of shock ionization by AGN winds in regions outside the AGN ionization structure, where shocked gas emission can be easily observed (Riffel et al. 2021a), and with the detection of a broad component in the integrated spectra shown in Fig. 7. On the other hand, the broad outflow component shows much higher  $[\text{O I}]\lambda 6300/H\alpha$  and  $\sigma_{\text{O I}}$  and there is a stronger correlation between these two parameters ( $R_p = 0.44$ ), which suggests that shock excitation is important in the production of emission of the outflowing gas.

Thus, the main excitation mechanism of the gas in the disc may be photoionization by the central AGN of UGC 8782 as indicated by the observed emission line ratios and kinematics, with an additional contribution of shocks. On the other hand, the enhanced gas emission associated with radio hotspots, the observed intensity line ratios, and the correlation between  $[\text{O I}]\lambda 6300/H\alpha$  and  $\sigma_{\text{O I}}$  indicate that shocks play an important role in the excitation of the gas in the outflow.

## 5.2 The disc component

The gas velocity field for the disc component (Fig. 3) shows a clear rotation pattern for all emission lines, with the line of nodes oriented approximately along the orientation of the major axis of the galaxy’s large-scale disc (PA =  $50^\circ$ ; Skrutskie et al. 2006). This behaviour is similar to that observed for the stars (Fig. 3) and in cold molecular gas, traced by the CO emission (Labiano et al. 2014). However, deviation from pure rotation is also observed in the ionized gas, as a discontinuity in velocities seen at  $\sim 1$  arcsec north-east of the nucleus. In order to better constrain the gas kinematics, we use the KINEMETRY method (Krajnovic et al. 2006) to model the gas velocity field from the  $H\alpha$  narrow component. This method is a generalization of the surface photometry technique and can be used to model the observed velocity field by a set of ellipses under the assumption that the velocity profile along each ellipse satisfies a cosine law, using the Fourier expansion technique (Krajnovic et al. 2006).

Fig. 8 shows, in the top panels, the observed  $H\alpha$  velocity field for the disc (narrow) component (left panel), the resulting best-fitting model obtained by the KINEMETRY method (central panel) and the residual map obtained by subtracting the model from the observed velocities (right panel). The bottom-left panel shows the radial variation of the kinematic position angle (PA) of the major axis of the fitted ellipses (in black) and the photometric PA (in red) obtained by modelling the continuum image (Fig. 3) using the

PHOTUTILS package (Bradley et al. 2020). The bottom-central and bottom-right panels show the harmonic coefficients  $k_1$  and  $k_5/k_1$ , respectively. The  $k_1$  term describes the velocity amplitude of bulk gas motions, while the  $k_5/k_1$  term quantifies higher order deviations from pure rotation (Krajinovic et al. 2006).

The photometric and kinematic PAs of the major axis of the ellipses approximately follow each other, with the highest offset of less than  $10^\circ$  observed at  $\sim 0.7$  arcsec and at 1.5 arcsec from the nucleus. These discrepancies are observed at the same distances of a redshifted structure north of the nucleus and an excess of blueshifts to the north-west of it, observed in the velocity field. The PA of the major axis changes from  $\Psi_0 = \sim 20^\circ$  close to the nucleus to  $\Psi_0 = \sim 50^\circ$  in the outer regions, becoming similar to the values derived for the large-scale disc using images in different bands (50–68°; Mackay 1971; Skrutskie et al. 2006; Adelman-McCarthy et al. 2008) and from the analysis of the kinematics of the cold gas (Labiano et al. 2014). The near side of the disc corresponds to the north-western side of the galaxy, where obscuration is higher (Floyd et al. 2006; Labiano et al. 2014). A higher extinction at the north-western side of the galaxy is also confirmed by our GMOS data in a map for the ratio between the red and blue stellar continuum, resulting in higher values to the north-western side of the disc.

The rotation curve (bottom central panel in Fig. 8) shows increasing velocity values outward from the nucleus, reaching a maximum value of  $\sim 130$  km s $^{-1}$ . The  $k_5/k_1$  parameter shows values close to zero in the inner  $\sim 1$  arcsec, and growing outwards, reaching a maximum value of  $\sim 0.15$ . This indicates that beyond the inner arcsec, the gas kinematics shows deviations that cannot be explained by regular rotation under the galaxy’s gravitational potential. The residual map (top-right panel of Fig. 8) shows low values ( $\lesssim 30$  km s $^{-1}$ ), but with a systematic pattern, supporting an additional kinematic component. Redshifted regions are observed approximately along the minor axis of the galaxy, while blueshifted residuals are seen mainly along the major axis of the galaxy. The complex gas kinematics observed in the disc component of UGC 8782 is likely produced by a merger event with a gas-rich galaxy, providing a gas reservoir to feed the central SMBH as suggested by previous studies (e.g. Evans et al. 1999; Martel et al. 1999; Beswick, Pedlar & Holloway 2002; Emonts et al. 2005).

We can estimate the mass of ionized gas in the disc by

$$M_{\text{ion}} = 1.4 N_e m_p V f, \quad (2)$$

where  $m_p$  is the mass of the proton,  $N_e$  is the electron density,  $V$  is the volume of the emitting gas, the 1.4 factor is included to account for the contribution of He, and  $f$  is the filling factor that can be obtained from

$$L_{\text{H}\alpha} \approx 4\pi j_{\text{H}\alpha} V f, \quad (3)$$

where  $L_{\text{H}\alpha}$  is the H $\alpha$  luminosity and  $4\pi j_{\text{H}\alpha}/N_e^2 = 3.558 \times 10^{-25}$  erg cm $^{-3}$  s $^{-1}$  assuming the case B H II recombination for the low-density limit and an electron temperature of 10 000 K (Osterbrock & Ferland 2006). Replacing  $f$  from equation (3) into equation (2), we obtain

$$M_{\text{ion}} \approx 7 \times \frac{L_{\text{H}\alpha}}{N_e}. \quad (4)$$

We calculate  $L_{\text{H}\alpha}$  from the H $\alpha$  fluxes for the disc component in each spaxel, after correcting them for extinction using the  $A_V$  map from Fig. 4 and the extinction law of Cardelli et al. (1989). For spaxels with no  $A_V$  estimates, we use the mean  $A_V$  value to correct the H $\alpha$  flux. Using the  $N_e$  values for the disc component and using their mean value in spaxels with no  $N_e$  measurements, we obtain

$M_{\text{ion}} = (1.1 \pm 0.4) \times 10^7 M_\odot$ . The mass of ionized gas in the disc is about three orders of magnitude lower than the mass of cold gas in UGC 8782, of  $2.2 \times 10^{10} M_\odot$  (Evans et al. 1999; Labiano et al. 2014).

### 5.3 Properties of the outflows

The geometry of the multiphase gas outflows in UGC 8782 is an intriguing question. Outflows in neutral gas are co-spatial with the western radio hotspot (Mahony et al. 2013), while previous studies of the ionized gas kinematics found that the highest velocity component arises from a region co-spatial with the eastern radio hotspot (Mahony et al. 2016). Shock-heated gas emission is detected in X-rays at the nucleus and inner radio jet, as well as in diffuse X-ray emission to the north and to the south of the nucleus (Lanz et al. 2015). The cold molecular counterpart of the outflows has not yet been detected, and IRAM Plateau de Bure interferometer observations of the CO emission give an upper limit of  $7.1 \times 10^8 M_\odot$  for the mass of the cold gas outflow (Labiano et al. 2014). The eastern side of the inner radio jet is approaching us making an angle of  $\sim 50^\circ$  with the line of sight (Beswick et al. 2004), consistent with the orientation of the galaxy such that the northwestern side is nearer to us. The inclination of the disc is  $i = 50 \pm 5^\circ$  (relative to the plane of the sky) as obtained from ellipse fitting of the continuum image and consistent with the large-scale disc ( $i \approx 53^\circ$ ; Skrutskie et al. 2006).

Mahony et al. (2016) interpreted the ionized gas outflows in UGC 8782 as being driven by the radio jet, and a cocoon structure surrounding the radio jet disturbing the gas in the central region of the galaxy. They found that the outflows are detected in blueshifts on both sides of the nucleus, with higher velocities observed to the eastern side attributed to the interaction of the approaching (eastern side) radio jet with the ambient gas. As shown in Fig. 7, our GMOS data reveal the presence of a blueshifted broad component not only at the position of the radio hotspots but also from regions away of the radio structure. In addition, the velocities of the outflow are similar at locations co-spatial with the eastern and western radio hotspots. As already noticed by Mahony et al. (2016), the flux of the broad component at the eastern hotspot is very low and marginally detected in their data, leading to a high uncertainty in the velocity of the outflow. Indeed, the example of line fits shown by these authors in their fig. 3 seems to slightly overestimate the blue wing of the [S II] lines leading to a higher inferred velocity, as compared with the most prominent outflow component detected at the location of the western radio hotspot.

In agreement with previous observations, our data also support a contribution of shock excitation of the gas in the outflow, as discussed above. The close association between the enhanced emission structures seen in ionized gas with the radio structures indicates that the shocks are produced by jet–cloud interaction. From the spectra extracted on selected locations (Fig. 7), we find that the outflow component is blueshifted at all positions, with the highest velocity observed for the nucleus. The outflows are seen in blueshifts at all locations surrounding the nucleus if they are produced by the cocoon created by the radio jet (Mahony et al. 2016), with the enhanced emission to the western side of the galaxy being produced by the interaction of the radio jet with the ambient gas of the galaxy. Enhanced emission-line widths in regions perpendicularly to the radio jet have been observed in nearby Seyfert galaxies, but with centroid velocities close to the systemic velocity of the galaxies, and interpreted as being due to jets perturbing the gas in the disc (e.g. Venturi et al. 2021; Girdhar et al. 2022), equatorial outflows

predicted by torus wind models (e.g. Elitzur 2012; Hönig et al. 2013; Riffel, Storchi-Bergmann & Riffel 2014), or due to much wider opening angle outflows as compared with the AGN ionization cones (e.g. Riffel et al. 2021a). The observed blueshifted velocities at all locations around the nucleus favour a scenario in which the ionized outflows in UGC 8782 present a spherical geometry, consistent with some theoretical predictions (Wagner, Bicknell & Umemura 2012; Ishibashi, Fabian & Reynolds 2019).

To compute the mass of ionized gas in the outflow, first we correct the flux of the  $H\alpha$  broad component at each spaxel using the  $A_V$  values (Fig. 4) for the broad component and the extinction law of Cardelli et al. (1989). For spaxels with no  $A_V$  estimations, we use its mean value. Then, we compute the mass of the gas in each spaxel using equation (4) and the observed  $N_e$  values for the outflow from Fig. 4 or its mean value for spaxels with no density measurements. Finally, we sum the mass contributions of all spaxels resulting in a mass of ionized gas in the outflow of  $M_{\text{out}} = (3.3 \pm 1.1) \times 10^6 M_{\odot}$ . This value corresponds to about 25 per cent of the total mass of ionized gas in the central region of UGC 8782.

We estimate the mass outflow rate and kinetic power of the ionized gas outflows within circular rings with width  $\Delta R = 0.3$  arcsec centred at the nucleus by

$$\dot{M}_{\text{out},\Delta R} = \sum_i \frac{M_{\text{out},\Delta R}^i V_{\text{out},\Delta R}^i}{\Delta R}, \quad (5)$$

and

$$\dot{K}_{\text{out},\Delta R} = \sum_i \frac{M_{\text{out},\Delta R}^i (V_{\text{out},\Delta R}^i)^3}{2\Delta R}, \quad (6)$$

where the sum is performed over velocity bins corresponding to the spectral sampling of the final data cube ( $\sim 45 \text{ km s}^{-1}$ ) with velocities in the range from  $-3000$  to  $3000 \text{ km s}^{-1}$ ,  $M_{\text{out},\Delta R}^i$  is the mass of ionized gas within the ring at the velocity channel  $i$ , and  $V_{\text{out},\Delta R}^i$  corresponds to the absolute value of the velocity of the outflow. We constructed velocity channel maps for the  $H\alpha$  outflow component, using a data cube constructed by subtracting the models of the stellar population contribution and of the narrow  $H\alpha$  component and the  $[\text{N II}]$  emission lines. To compute the mass within each channel and radial bin, we adopt the mean electron density value for the outflow component. Fig. 9 presents the resulting radial profiles of mass outflow rate (top panel) and kinetic power of the outflows (bottom panel). The error bars correspond to the uncertainties propagated from the flux, velocity, and electron density. The peaks of  $\dot{M}_{\text{out},\Delta R}$  and  $\dot{K}_{\text{out},\Delta R}$  occur at  $\sim 1$  arcsec, as expected by the enhanced emission at the location of the western radio hotspot, reaching values of  $0.5 \pm 0.1 M_{\odot} \text{ yr}^{-1}$  and  $(6.8 \pm 1.1) \times 10^{41} \text{ erg s}^{-1}$ , respectively. These are the lower limits because where there is ionized gas, there must be neutral gas as well because otherwise the clouds get overionized to a much higher ionization level than observed (Dempsey & Zakamska 2018). The peak mass outflow rate derived here is about three times larger than the value derived by Mahony et al. (2016). This discrepancy is due to the different assumptions by these authors and in this work, and specifically due to the correction of the  $H\alpha$  fluxes for extinction, not performed in the previous work. The kinetic power of the outflows is about two orders of magnitude smaller than the kinetic power of the radio jets in UGC 8782, of  $2\text{--}4 \times 10^{43} \text{ erg s}^{-1}$  (Lanz et al. 2015), consistent with a jet-driven outflow.

We estimate the AGN bolometric luminosity ( $L_{\text{bol}}$ ) from the  $[\text{O III}]\lambda 5007$  luminosity by  $L_{\text{bol}} = 3500 L_{[\text{O III}]}$  (Heckman et al. 2004). Using the integrated  $[\text{O III}]\lambda 5007$  luminosity, corrected by

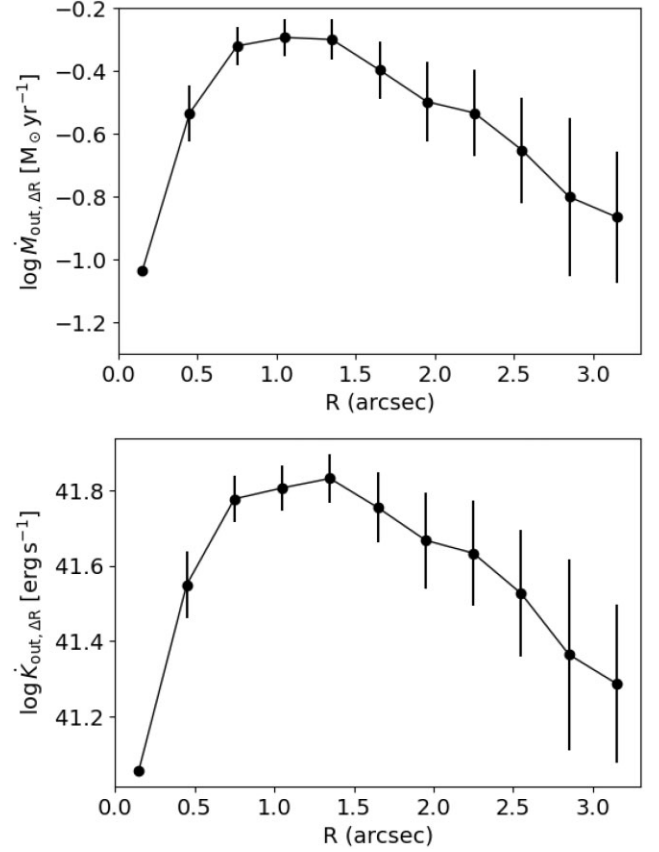


**Figure 9.** Radial profiles of the mass outflow rate (top panel) and kinetic power (bottom panel) of the ionized outflows in UGC 8782.

dust extinction, using the law of Cardelli et al. (1989), we obtain  $L_{\text{bol}} = (2.2 \pm 0.7) \times 10^{43} \text{ erg s}^{-1}$ . Using the relation of  $L_{\text{bol}}$  with the  $H\alpha$  luminosity,  $L_{\text{bol}} = 2000 L_{H\alpha}$  (Sikora et al. 2013), the resulting bolometric luminosity is  $L_{\text{bol}} = (2.5 \pm 0.4) \times 10^{43} \text{ erg s}^{-1}$ . Finally, using the hard X-ray bolometric correction from Netzer (2019) and the observed 2–10 keV flux from Ueda et al. (2005), we obtain  $L_{\text{bol}} \approx 7.2 \times 10^{43} \text{ erg s}^{-1}$ . An advantage of using X-ray observations is that it is less sensitive to dust obscuration and to scattered or reprocessed emission than optical wavelengths, being a direct tracer of the AGN emission.

The kinetic power of the ionized outflows corresponds to  $\sim 1\text{--}3$  per cent of the bolometric luminosity of the AGN in UGC 8782, depending on the tracer used to estimate the bolometric luminosity. This indicates that the ionized gas outflows could be powerful enough to suppress the star formation in the host galaxy as the kinetic coupling efficiency of the outflow is larger than the minimum value required by simulations for AGN feedback to have an effective impact on the host galaxies (e.g. Di Matteo et al. 2005; Hopkins & Elvis 2010; Dubois et al. 2014; Schaye et al. 2015; Weinberger et al. 2017; Harrison et al. 2018). In addition, the kinetic energy of the outflows represents less than 20 per cent of the total energy released by the outflow and the contribution from the other gas phases is expected to be non-negligible (Richings & Faucher-Giguère 2018b). On the other hand, it is worth mentioning that the uncertainties in the outflow properties are usually high (up to two orders of magnitude), due to assumptions on their densities and geometry (Davies et al. 2020; Molina et al. 2022; Revalski et al. 2022; Riffel et al. 2023).

## 6 CONCLUSIONS

We used GMOS-IFU observations of the radio loud AGN host UGC 8782 at a spatial resolution of  $\sim 725$  pc to study the gas emission structure and kinematics in the inner  $3.4 \times 4.9$  kpc<sup>2</sup> of the galaxy. Our main conclusions are as follows:

(i) The emitting gas presents high-velocity dispersion as quantified by the  $W_{30}$  maps, with values larger than  $500 \text{ km s}^{-1}$  at several locations. The highest values are observed west ( $\sim 1$  kpc) of the nucleus in regions co-spatial with the inner radio jet, indicating a jet–cloud interaction.

(ii) The profiles of each emission line are fitted by two Gaussian curves: a narrow ( $\sigma \lesssim 200 \text{ km s}^{-1}$ ) and a broad ( $\sigma \gtrsim 200 \text{ km s}^{-1}$ ) component. The narrow component traces the emission of the gas in the galaxy disc, while the broad component is consistent with gas outflows.

(iii) The narrow component gas kinematics shows a pattern of disc rotation, similar to that of the stars. However, differences between the observed  $H\alpha$  velocity field and a rotation disc model of up to  $30 \text{ km s}^{-1}$  are also present, likely associated with disturbed gas kinematics due to a previous galaxy merger process.

(iv) The broad component is blueshifted by  $\sim 150$ – $500 \text{ km s}^{-1}$  relative to the systemic velocity of the galaxy and has a velocity dispersion of up to  $\sigma \approx 400 \text{ km s}^{-1}$ . This component is detected for individual spaxels mainly at locations to the west and north of the nucleus, but it is observed in integrated spectra at several locations surrounding the nucleus.

(v) The BPT and WHAN diagnostic diagrams show that both disc and outflow components present values in the AGN region. Shock gas excitation is also supported for the outflow component by the enhanced emission co-spatial with the western radio hotspot and by a correlation between  $[O\text{I}] \lambda 6300/H\alpha$  and  $\sigma_{O\text{I}}$ , known shock tracers.

(vi) We estimate the mass outflow rate and kinetic power of the ionized gas outflows at different distances from the nucleus. The highest values of these properties are observed at  $\sim 1$  kpc from the nucleus with values of  $\dot{M}_{\text{out},\Delta R} = 0.5 \pm 0.1 M_{\odot} \text{ yr}^{-1}$  and  $\dot{K}_{\text{out},\Delta R} = (6.8 \pm 1.1) \times 10^{41} \text{ erg s}^{-1}$ . The kinetic power of the outflows corresponds to 1–3 per cent of the AGN bolometric luminosity.

## ACKNOWLEDGEMENTS

We thank to an anonymous referee for their constructive comments that helped improve this manuscript. Based on observations obtained at the Gemini Observatory, which is operated by the Association of Universities for Research in Astronomy, Inc., under a cooperative agreement with the NSF on behalf of the Gemini partnership: the National Science Foundation (United States), National Research Council (Canada), CONICYT (Chile), Ministerio de Ciencia, Tecnología e Innovación Productiva (Argentina), Ministério da Ciência, Tecnologia e Inovação (Brazil), and Korea Astronomy and Space Science Institute (Republic of Korea). This research has made use of NASA's Astrophysics Data System Bibliographic Services. This research has made use of the NASA/IPAC Extragalactic Database (NED), which is operated by the Jet Propulsion Laboratory, California Institute of Technology, under contract with the National Aeronautics and Space Administration. RAR acknowledges the support from Conselho Nacional de Desenvolvimento Científico e Tecnológico (CNPq) and Fundação de Amparo à pesquisa do Estado do Rio Grande do Sul (FAPERGS). RR thanks to CNPq (Proj. 311223/2020-6, 304927/2017-1, and 400352/2016-8) and FAPERGS (Proj. 16/2551-0000251-7 and 19/1750-2). MB and GLSO thank to Coordenação

de Aperfeiçoamento de Pessoal de Nível Superior (CAPES; Proj. 0001).

## DATA AVAILABILITY

The processed data used in this article will be shared on reasonable request to the corresponding author.

## REFERENCES

- Adelman-McCarthy J. K. et al., 2008, *ApJS*, 175, 297  
 Agostino C. J. et al., 2021, *ApJ*, 922, 156  
 Allen M. G., Groves B. A., Dopita M. A., Sutherland R. S., Kewley L. J., 2008, *ApJS*, 178, 20  
 Allington-Smith J. et al., 2002, *PASP*, 114, 892  
 Alonso-Herrero A. et al., 2019, *A&A*, 628, A65  
 Baldwin J. A., Phillips M. M., Terlevich R., 1981, *PASP*, 93, 5  
 Beswick R. J., Pedlar A., Holloway A. J., 2002, *MNRAS*, 329, 620  
 Beswick R. J., Peck A. B., Taylor G. B., Giovannini G., 2004, *MNRAS*, 352, 49  
 Bianchin M. et al., 2022, *MNRAS*, 510, 639  
 Bradley L. et al., 2020, *astropy/photutils: 1.0.0*, <https://doi.org/10.5281/zenodo.4044744>  
 Cappellari M., 2017, *MNRAS*, 466, 798  
 Cappellari M., 2022, preprint ([arXiv:2208.14974](https://arxiv.org/abs/2208.14974))  
 Cappellari M., Emsellem E., 2004, *PASP*, 116, 138  
 Cappellari M., Verolme E. K., van der Marel R. P., Verdoes Kleijn G. A., Illingworth G. D., Franx M., Carollo C. M., de Zeeuw P. T., 2002, *ApJ*, 578, 787  
 Cardelli J. A., Clayton G. C., Mathis J. S., 1989, *ApJ*, 345, 245  
 Chambers K. C. et al., 2016, preprint ([arXiv:1612.05560](https://arxiv.org/abs/1612.05560))  
 Cid Fernandes R., Stasińska G., Schlickmann M. S., Mateus A., Vale Asari N., Schoenell W., Sodré L., 2010, *MNRAS*, 403, 1036  
 Cid Fernandes R., Stasińska G., Mateus A., Vale Asari N., 2011, *MNRAS*, 413, 1687  
 Comerón S., Knapen J. H., Ramos Almeida C., Watkins A. E., 2021, *A&A*, 645, A130  
 Couto G. S., Storchi-Bergmann T., Siemiginowska A., Riffel R. A., Morganti R., 2020, *MNRAS*, 497, 5103  
 Dall'Agnol de Oliveira B. et al., 2021, *MNRAS*, 504, 3890  
 Davies R. I. et al., 2014, *ApJ*, 792, 101  
 Davies R. et al., 2020, *MNRAS*, 498, 4150  
 Dempsey R., Zakamska N. L., 2018, *MNRAS*, 477, 4615  
 Di Matteo T., Springel V., Hernquist L., 2005, *Nature*, 433, 604  
 Dors O. L., Maiolino R., Cardaci M. V., Hägele G. F., Krabbe A. C., Pérez-Montero E., Armah M., 2020, *MNRAS*, 496, 3209  
 Dors O. L., Contini M., Riffel R. A., Pérez-Montero E., Krabbe A. C., Cardaci M. V., Hägele G. F., 2021, *MNRAS*, 501, 1370  
 Dubois Y. et al., 2014, *MNRAS*, 444, 1453  
 Elitzur M., 2012, *ApJ*, 747, L33  
 Emonts B. H. C., Morganti R., Tadhunter C. N., Oosterloo T. A., Holt J., van der Hulst J. M., 2005, *MNRAS*, 362, 931  
 Evans A. S., Sanders D. B., Surace J. A., Mazzarella J. M., 1999, *ApJ*, 511, 730  
 Fabian A. C., 2012, *ARA&A*, 50, 455  
 Feruglio C., Maiolino R., Piconcelli E., Menci N., Aussel H., Lamastra A., Fiore F., 2010, *A&A*, 518, L155  
 Feruglio C. et al., 2015, *A&A*, 583, A99  
 Fischer T. C. et al., 2017, *ApJ*, 834, 30  
 Flewelling H. A. et al., 2016, preprint ([arXiv:1612.05243](https://arxiv.org/abs/1612.05243))  
 Floyd D. J. E., Perlman E., Leahy J. P., Beswick R. J., Jackson N. J., Sparks W. B., Axon D. J., O'Dea C. P., 2006, *ApJ*, 639, 23  
 Girdhar A. et al., 2022, *MNRAS*, 512, 1608  
 Harrison C. M., Costa T., Tadhunter C. N., Flütsch A., Kakkad D., Perna M., Vietri G., 2018, *Nat. Astron.*, 2, 198  
 Heckman T. M., Kauffmann G., Brinchmann J., Charlot S., Tremonti C., White S. D. M., 2004, *ApJ*, 613, 109

- Hill M. J., Zakamska N. L., 2014, *MNRAS*, 439, 2701
- Ho I. T. et al., 2014, *MNRAS*, 444, 3894
- Hönig S. F. et al., 2013, *ApJ*, 771, 87
- Hook I. M., Jørgensen I., Allington-Smith J. R., Davies R. L., Metcalfe N., Murowinski R. G., Crampton D., 2004, *PASP*, 116, 425
- Hopkins P. F., Elvis M., 2010, *MNRAS*, 401, 7
- Ishibashi W., Fabian A. C., Reynolds C. S., 2019, *MNRAS*, 486, 2210
- Kauffmann G. et al., 2003, *MNRAS*, 346, 1055
- Kewley L. J., Dopita M. A., Sutherland R. S., Heisler C. A., Trevena J., 2001, *ApJ*, 556, 121
- Kormendy J., Ho L. C., 2013, *ARA&A*, 51, 511
- Krajinovic D., Cappellari M., De Zeeuw P. T., Copin Y., 2006, *MNRAS*, 366, 787
- Kukreti P. et al., 2022, *A&A*, 658, A6
- Labiano A. et al., 2014, *A&A*, 564, A128
- Lambrides E. L., Petric A. O., Tchernyshyov K., Zakamska N. L., Watts D. J., 2019, *MNRAS*, 487, 1823
- Lanz L., Ogle P. M., Evans D., Appleton P. N., Guillard P., Emonts B., 2015, *ApJ*, 801, 17
- Liu F. K., Zhang Y. H., 2002, *A&A*, 381, 757
- Liu G., Zakamska N. L., Greene J. E., Nesvadba N. P. H., Liu X., 2013, *MNRAS*, 436, 2576
- Luridiana V., Morisset C., Shaw R. A., 2015, *A&A*, 573, A42
- Machalski J., Jamrozny M., Stawarz Ł., Weżgowiec M., 2016, *A&A*, 595, A46
- Mackay C. D., 1971, *MNRAS*, 151, 421
- Mahony E. K., Morganti R., Emonts B. H. C., Oosterloo T. A., Tadhunter C., 2013, *MNRAS*, 435, L58
- Mahony E. K., Oonk J. B. R., Morganti R., Tadhunter C., Bessiere P., Short P., Emonts B. H. C., Oosterloo T. A., 2016, *MNRAS*, 455, 2453
- Martel A. R. et al., 1999, *ApJS*, 122, 81
- May D., Steiner J. E., 2017, *MNRAS*, 469, 994
- Molina J. et al., 2022, *ApJ*, 935, 72
- Monreal-Ibero A., Arribas S., Colina L., 2006, *ApJ*, 637, 138
- Monreal-Ibero A., Arribas S., Colina L., Rodríguez-Zaurín J., Alonso-Herrero A., García-Marín M., 2010, *A&A*, 517, A28
- Morganti R., Oosterloo T. A., Emonts B. H. C., van der Hulst J. M., Tadhunter C. N., 2003, *ApJ*, 593, L69
- Netzer H., 2019, *MNRAS*, 488, 5185
- Osterbrock D. E., Ferland G. J., 2006, *Astrophysics of Gaseous Nebulae and Active Galactic Nuclei*. University Science Books, Mill Valley, CA
- Ramos Almeida C., Piqueras López J., Villar-Martín M., Bessiere P. S., 2017, *MNRAS*, 470, 964
- Revalski M., Crenshaw D. M., Kraemer S. B., Fischer T. C., Schmitt H. R., Machuca C., 2018a, *ApJ*, 856, 46
- Revalski M. et al., 2018b, *ApJ*, 867, 88
- Revalski M. et al., 2021, *ApJ*, 910, 139
- Revalski M. et al., 2022, *ApJ*, 930, 14
- Rich J. A., Kewley L. J., Dopita M. A., 2011, *ApJ*, 734, 87
- Rich J. A., Kewley L. J., Dopita M. A., 2015, *ApJS*, 221, 28
- Richings A. J., Faucher-Giguère C.-A., 2018a, *MNRAS*, 474, 3673
- Richings A. J., Faucher-Giguère C.-A., 2018b, *MNRAS*, 478, 3100
- Riffel R. A., 2021, *MNRAS*, 506, 2950
- Riffel R. A., Storchi-Bergmann T., Winge C., Barbosa F. K. B., 2006, *MNRAS*, 373, 2
- Riffel R. A., Storchi-Bergmann T., Riffel R., 2014, *ApJ*, 780, L24
- Riffel R. A., Zakamska N. L., Riffel R., 2020a, *MNRAS*, 491, 1518
- Riffel R. A., Storchi-Bergmann T., Zakamska N. L., Riffel R., 2020b, *MNRAS*, 496, 4857
- Riffel R. A. et al., 2021a, *MNRAS*, 501, L54
- Riffel R. et al., 2021b, *MNRAS*, 501, 4064
- Riffel R. A. et al., 2021c, *MNRAS*, 504, 3265
- Riffel R. A., Dors O. L., Krabbe A. C., Esteban C., 2021d, *MNRAS*, 506, L11
- Riffel R. A. et al., 2023, *MNRAS*, 521, 1832
- Rupke D. S. N. et al., 2019, *Nature*, 574, 643
- Ruschel-Dutra D., de Oliveira B. D., 2020, *danielrd6/ifscube v1.0*.
- Ruschel-Dutra D. et al., 2021, *MNRAS*, 507, 74
- Sandage A., 1966, *ApJ*, 145, 1
- Schaye J. et al., 2015, *MNRAS*, 446, 521
- Shimizu T. T. et al., 2019, *MNRAS*, 490, 5860
- Sikora M., Stasińska G., Koziel-Wierzbowska D., Madejski G. M., Asari N. V., 2013, *ApJ*, 765, 62
- Skrutskie M. F. et al., 2006, *AJ*, 131, 1163
- Speranza G. et al., 2022, *A&A*, 665, A55
- Ueda Y., Ishisaki Y., Takahashi T., Makishima K., Ohashi T., 2005, *ApJS*, 161, 185
- van Dokkum P. G., 2001, *PASP*, 113, 1420
- Venturi G. et al., 2021, *A&A*, 648, A17
- Véron-Cetty M. P., Véron P., 2006, *A&A*, 455, 773
- Wagner A. Y., Bicknell G. V., Umemura M., 2012, *ApJ*, 757, 136
- Weinberger R. et al., 2017, *MNRAS*, 465, 3291
- Westfall K. B. et al., 2019, *Astron. J.*, 158, 231
- Wylezalek D., Flores A. M., Zakamska N. L., Greene J. E., Riffel R. A., 2020, *MNRAS*, 492, 4680
- Zakamska N. L., Greene J. E., 2014, *MNRAS*, 442, 784

This paper has been typeset from a  $\text{\TeX}/\text{\LaTeX}$  file prepared by the author.